Prediction of Feasibility of Polaronic OER on (110) Surface of Rutile TiO_2

Hori Pada Sarker[1,2,3], *Frank Abild-Pedersen*[1,3], and *Michal Bajdich*[1,3*]

[1]*Liquid Sunlight Alliance (LiSA)*
California Institute of Technology, Pasadena, CA 91125, USA

[2]*Department of Chemical Engineering, Stanford University*
443 Via Ortega, Stanford, CA 94305, USA

[3]*SUNCAT Center for Interface Science and Catalysis*
SLAC National Accelerator Laboratory
2575 Sand Hill Road, Menlo Park, CA 94025, USA

[*]*Corresponding e-mail address: bajdich@slac.stanford.edu*

ABSTRACT

The polaronic effects at the atomic level hold paramount significance for advancing the efficacy of transition metal oxides in applications pertinent to renewable energy. The lattice-distortion mediated localization of photoexcited carriers in the form of polarons plays a pivotal role in the photocatalysis. This investigation focuses on rutile TiO_2, an important material extensively explored for solar energy conversion in artificial photosynthesis, specifically targeting the generation of green H_2 through photoelectrochemical (PEC) H_2O splitting. By employing Hubbard-U corrected and hybrid density functional theory (DFT) methods, we systematically probe the polaronic effects in the catalysis of oxygen evolution reaction (OER) on the (110) surface of rutile TiO_2. Theoretical understanding of polarons within the surface, coupled with simulations of OER at distinct titanium (Ti) and oxygen (O) active sites, reveals diverse polaron formation energies within the lattice sites with strong preference for bulk and surface bridge (O_b) oxygen sites. Moreover, we provide the evidence for the facilitative role of polarons in OER. We find that hole polarons situated at the equatorial oxygen sites near the Ti - active site, along with bridge site hole polarons distal from the O_b active site yield a small reduction in OER overpotential by ~0.06eV and ~0.12eV, respectively. However, subsurface, equatorial, and bridge site hole polarons significantly reduce the Ti-active site OER overpotential by ~0.4eV through the peroxo-type oxygen pathway. We also observe that the presence of hole polarons stabilizes the *OH, *O, and *OOH intermediate species compared to the scenario without hole polarons. Overall, this study provides a detailed mechanistic insight into polaron-mediated OER, offering a promising avenue for improving the catalytic activity of transition metal oxide-based photocatalysts catering to renewable energy requisites.

Key words: Solar fuel, Hydrogen, Rutile TiO_2, Polaron, Density Functional Theory (DFT)

INTRODUCTION

Capturing solar photons and converting them into chemical energy, such as fuels, represents one of the promising pathways to mitigate environmental and climate catastrophes, achieve energy

security and independence, and establish a sustainable global economy, as demonstrated by numerous studies[1–5]. This is the underlying reason why researchers worldwide are actively working on the advancement of solar-driven fuel generation technologies. These endeavors include artificial photosynthesis aimed at producing environmentally friendly hydrogen (H_2) and solar-driven reduction of CO_2 into energy-dense fuels such as ethanol[6–8]. At the core of these solar-driven technologies, photoactive semiconducting materials play a crucial role in capturing solar photons and storing their energy within the chemical bonds of such fuels. Among the multitude of available photo-absorber materials, photo-active transition metal oxides (TMO's) stand out for their exceptional solar energy harvesting capabilities. With over 200 suitable photo-active TMO options, these materials have demonstrated potential for solar energy harvesting[9,10].

Among all TMO's, TiO_2 is one of the most studied photoanode materials for PEC water splitting[11]. TiO_2 has become a benchmarked material for understanding PEC water splitting due to its photo response within the UV and some part of the visible spectrum, high crystallinity, stability in aqueous solution, resistant to (photo) corrosion, non-toxicity, abundance and low cost[12,13]. Despite being one of the most widely studied photo-active materials, TiO_2 has major drawbacks in terms of UV-adsorption spectrum, carrier transport, particularly for efficient extraction and utilization of photogenerated charge carriers which eventually contribute to the higher overpotential associated with OER[14]. In fact, carrier transport limitation phenomenon is prevalent almost all the TMO based photocatalysts[15,16]. Poor carrier separation, carrier recombination, and slow carrier transfer kinetics are considered as the major efficiency loss channels among others.

In TiO_2 as well as other TMO's, slow moving carriers induce strong carrier-lattice interaction and subsequently distorts the lattice locally. Such a local distortion in lattice forms an attractive potential well within which slow moving carriers get trapped, interact with phonons, and eventually form polarons. Formation of polarons in TiO_2 as well as other TMO's are well established both experimentally[17–22] and theoretically[23–32]. The review paper by Franchini et al.[28] provided a list of polaron forming materials along with the characterization techniques employed in these studies. Polaron formation, dynamic nanoscale lattice distortion, as well as the associated strain field, all are central aspects of photocatalysis and play a crucial role in

photocatalytic chemical reactions[33]. However, the role of polarons in photocatalysis is quite unclear and not well studied.

In light of this, we studied hole polarons on a prototypical rutile TiO_2 (110) model surface using first principles density functional theory to understand whether it has any effects on OER catalytic activity. In a recent study, Gono et al.[27] reported a slight reduction of OER overpotential on the rutile TiO_2 (110) surface. They concluded that the OER overpotential reduction happens due to the presence of surface hole polarons. Inspired by this study, we conducted a thorough investigation, focusing specifically on the differences between the polaronic and non-polaronic OER, the types of polaronic sites that exists, and their overall effect on OER overpotential. We addressed the above questions by estimating polaronic stability, calculating polaronic electronic structure, the OER free energy landscape as well as the OER catalytic activity in terms of an OER volcano plot. We shall explain the concept in detail later. The OER on TiO_2 surface is a well-established chemical process, with numerous studies documented in the scientific literature[12,26,27,34],[35].

However, there is a lack of research examining the OER mechanism on the TiO_2 surface when there is polaron. In fact, there are very few studies which studied polaronic effects in photo-driven catalysis. Cheng et al.[36] reported enhanced electron polaron activity in rutile TiO_2 (110) surface upon CO adsorption during CO_2RR. They demonstrated that CO adsorption drives subsurface electron polarons towards the surface-active sites, thus making them chemically active. Guzelturk et al.[37] reported that local distortion or phonon cloud associated with the polarons enhances the carrier mobility in photovoltaic lead halide perovskites by protecting them from scattering off from defect centers. Contrary, Lohaus et al.[38] in their hematite (α-Fe_2O_3) paper postulated polaron induced photovoltage limitation by Fermi level pinning, hence PEC water splitting efficiency limitation, by measuring quasi-Fermi level splitting. Wiktor et al.[39] demonstrated that polaronic levels affect the alignment at the solid-liquid interface, and the carrier recombination happens via polarons in the PEC water splitting reaction. Rettie et al.[40] found a significant reduction of carrier mobility in W doped $BiVO_4$ by polarons. So, in light of this, it becomes highly crucial to gain a more profound understanding at the atomic level regarding the OER mechanism involving polarons. In addition, exploring any potential connections between polarons and the photocatalytic performance become important. This knowledge is essential not only to address the

efficiency limitations but also to formulate a cost-effective approach and propose efficient photocatalytic materials aimed at producing sustainable and renewable solar fuels.

In this study, we present a detailed characterization of polaron formation using Hubbard-U-corrected and hybrid density functional theory (DFT) calculations. We investigate polaron stability at various positions within the bulk and on the surface of TiO_2 via thermodynamic free energy calculations, as well as estimate the band-alignment energetics of polaronic states within the band gap. Additionally, we analyze the free energy landscape of OER as well as compare the catalytic activity with and without the presence of hole polarons. Finally, we discuss our calculated data in context of available experimental results.

COMPUTATIONAL METHODS

We performed spin polarized density functional theory (DFT) calculations using the Vienna ab initio Simulation Package (VASP-5.4.4)[41] within the python-based atomic simulation environment (ASE)[42]. The exchange and correlations were described by the Perdew-Burke-Ernzerhof (PBE) functional within the generalized gradient approximation (GGA)[43], and hybrid and Hubbard-U corrections were applied as discussed below. Projector-augmented plane wave (PAW)[44] method with a kinetic energy cut-off of 500 eV was used to treat the ion-electron interaction throughout all calculations, which gave well converged results. Our approach involved utilizing TiO_2 (110) surfaces: a (2×2) 4 - layers surface containing 96 atoms, a (2×2) 6 – layers surface containing 144 atoms, and a (4×2) 4 - layers surface containing 192 atoms. These surfaces were used to model hole polaron and simulate OER at Ti_{cus} (coordinatively unsaturated Ti - site) and O_b (bridge O - site) active sites, respectively. We obtained these above-mentioned surfaces from an optimized bulk structure. For bulk calculations, we used a (2×2×2) supercell containing 48 atoms and employed a 5×5×7 k-point grid for geometry optimization. For all surface calculations, at least 20 Å vacuum was employed between the repeating slabs in order to avoid spurious image-charge interactions. The bottom two layers were kept fixed to bulk geometry and top two layers as well as adsorbates (*OH, *O, and *OOH) were allowed to relax in all directions during surface geometry optimization below the force threshold of 0.02 $eVÅ^{-1}$. The k-point mesh was sampled using the Mohkhorst-Pack scheme. For geometry optimization and polaron localization in (2×2) 4-layers and (2×2) 6-layers surfaces, a 7×3×1 k-point grid was employed. For the (4×2) 4 -layers surface, a 3×3×1 k-point grid was utilized. To model hole polaron, we introduce

an additional hole to the relaxed surface. Along with adding the extra hole, we initially introduced a small perturbation around the site of the polaron to break the local lattice symmetry before proceeding structural relaxation. Furthermore, to maintain charge neutrality of the surface, we incorporated a compensating homogeneous background counter charge as implemented by VASP. Finally, we characterized polaron formation by analyzing the polaron footprints (e.g., iso-surface charge density, local lattice distortion, polaronic electronic state within the bandgap in the density of states plot, and localized spin magnetic moment at polaronic site) within the fully relaxed structure which is explained in detail in the next section. Additionally, polaron formation energy was calculated using the following formula[23].

$$E_{pol}^{\pm} = E^{polaron}(N \mp 1) - E^{perf}(N \mp 1), \qquad (1)$$

where $E_{pol}^{\pm}$ is the polaron formation energy and (+) sign corresponds to hole polaron, while (-) sign corresponds to electron polaron. A negative $E_{pol}^{\pm}$ implies energy gain and hence formation of a stable polaron. $E^{polaron}$ and E^{perf} are the estimated PBE+U total energies of the relaxed system with extra charge in polaronic (distorted geometry) and non-polaronic (undistorted) geometry, respectively. E^{perf} calculations were performed on a completely relaxed system, forcing delocalization of holes. The number of electrons is given in parenthesis, where *N* represents total number of electrons of the neutral system. $E_{pol}^{\pm}$ is the outcome of interplay between the energy needed to deform the lattice locally to accommodate hole polaron (E_{ST}), and the electronic energy gain due to the localization of hole within the distorted lattice (E_{EL}). The detail of the $E_{pol}^{\pm}$ calculation method is outlined elsewhere[23].

DFT is known to underestimate electron self-interaction corrections (SIC)[45–47]. Due to the SIC errors, DFT often fails to produce a desired localized polaronic solution. Hybrid density functional as well as Hubbard U correction can overcome the SIC error. To address the charge delocalization issue present in the standard DFT method, we implemented a Hubbard-U correction targeting the atoms where polarons are localized. We also employed hybrid density functional (HSE06)[48] method to benchmark the U value applied in this study (**Figure S1**). In HSE06 calculations, a 25% HF exchange was employed, producing a band gap close to the experimental value (3.0 eV)[13,49,50] (**Figure S2**). Similar to Deskins et al.[30], an effective U value (U_{eff}) of 10 eV to O 2p-orbital at polaronic site was employed [25,29,30,51]. Deskins et al.[30] previously

benchmarked the U value for hole polaron formation at O-site in rutile TiO_2. They demonstrated that at lower U values (U < 10 eV), it is difficult to localize hole polaron at O-site. However, using U_{eff} of 10 eV, they successfully localized hole polaron at O-site and estimated hole polaron mobility which is in good agreement with experiment. Furthermore, the position of hole polaronic state within the band gap, estimated by employing U_{eff} of 10 eV, closely aligns with the HSE06 prediction (**Figure S3**). In other compounds such as in $BiVO_4$, Pasumarthi et al.[52] and Liu et al.[53] applied an U_{eff} value of 9 eV to localize hole polaron at a single oxygen atom. Additionally, Liu et al. showed that U_{eff} = 9 eV satisfied the behavior of piece-linearity of DFT energies with respect to fractional occupation in $BiVO_4$.

For electron localization at Ti^{+3} - site in rutile TiO_2, many studies applied U_{eff} values ranging from (3.3-5.5) eV[17,24,29,51,54]. For example, Deskins et al.[29] applied an U_{eff} value of 4.1eV to localize electron polaron at Ti - site in rutile TiO_2. Stevin et al.[17] applied an U_{eff} value of 3.9 eV to generate stable electron polaron on defect free rutile TiO_2 (110) surface. Selcuk et al.[24] also applied a similar value of U_{eff} = 3.9 eV to localize electron polaron on anatase (101) and (001) surfaces. Calzado et al.[54] applied a U_{eff} = 5.5 eV to localize electron polaron on the reduced rutile TiO_2 surface. They demonstrated that the electron polaronic state is located ~1 eV below the conduction band edge, as reported in many published literatures[26,55]. The position of polaronic state within band gap is an important electronic feature, and, as demonstrated by Calzado et al.[54], U_{eff} = 5.5 eV can accurately predict the electron polaronic state in rutile TiO_2. Due to this, in this study, we also applied a U_{eff} = 5.5 eV to Ti 3d orbitals, similar to Calzado et al.[54], to localize electron polaron on reduced rutile TiO_2 surface. Moreover, the U_{eff} values in this study successfully reproduced our hybrid DFT calculated magnetic moment (~0.75 μ_B for electron and ~ 0.68 μ_B for hole polaron). Additionally, they accurately predicted the position of the hole polaronic state within the band gap for TiO_2 bulk (**Figure S3**).

RESULTS AND DISCUSSIONS

Hole polaron in the bulk of rutile TiO_2

In this study, we considered rutile phase of TiO_2 [Tetragonal; $P4_2/mnm$; a = b = 4.66Å (exp[50]=4.58Å), c = 2.97Å (exp[50]=2.95Å)] and its (110) surface was derived from the optimized unit cell according to the Computational Methods section and SI **Figure S4**.

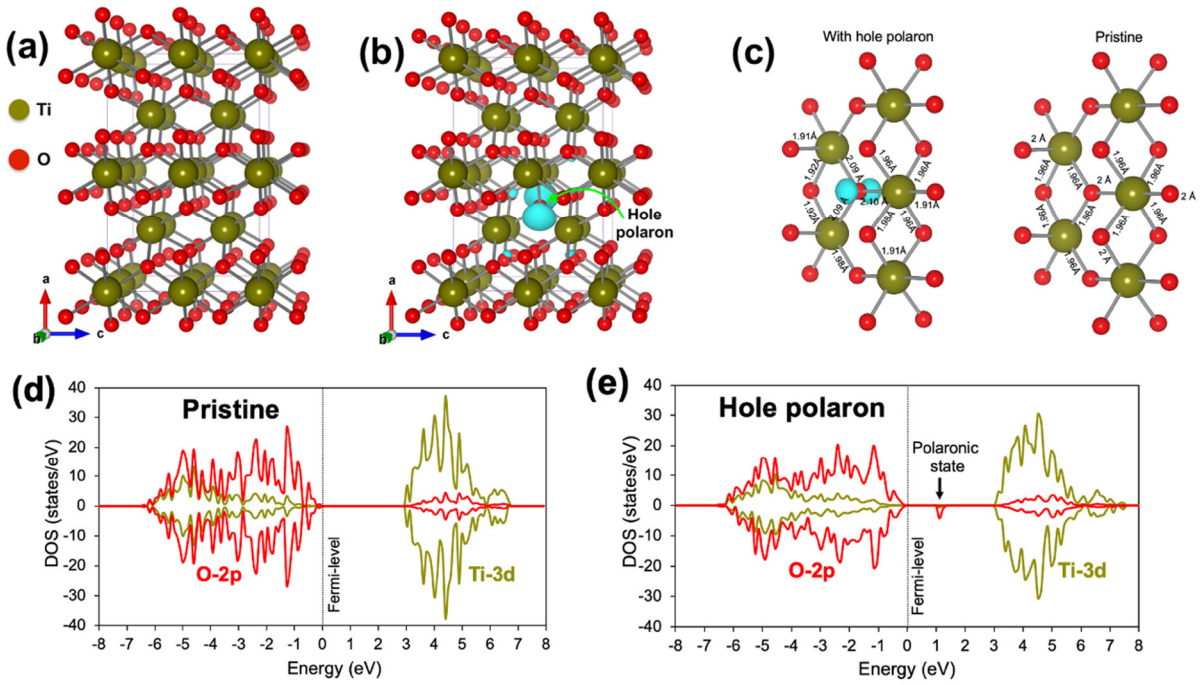

***Figure 1**. Fully DFT optimized ball and stick structural models of (a) TiO_2 bulk crystal structure and (b) bulk hole polaron at O-site. The iso-surfaces (azure blue color) indicate the hole polaron at oxygen site at value of 0.005 eÅ^{-3}. (c) Comparison of the local distortion with and without hole polaron. (d) Density of states (DOS) for pristine bulk and (e) for bulk hole polaron. For both case, DOS are calculated using hybrid density functional level of DFT (HSE06).*

Figure 1a shows the optimized bulk while **Figure S4** shows the corresponding (110) surface geometry. TiO_2 (110) surface has two distinct type of Ti atoms. They are five coordinated Ti_{cus} (coordinatively unsaturated site) and six coordinated Ti_{css} (coordinatively saturated site) sites. Similar to Ti – atoms, surface oxygen atoms also have two distinctive classifications: two coordinated bridge oxygen (O_b) and three coordinated planar oxygen (O_p). And hole polarons in rutile TiO_2 form at O – atoms. In fact, in strongly correlated systems i.e., TiO_2 as well as other TMO's[28], polaron formation is a ubiquitous phenomenon. Due to strong carrier-lattice interaction, photoexcited or defect generated charge carriers interact and strongly couple with optical phonons, and hence form polarons. It is well established experimentally[18,20,21,56] and theoretically[17,23,28–32] that TiO_2 forms polaron. An electron polaron forms at Ti – sites and a hole polaron at O – sites. The rationale behind the site selectivity of polaron formation in TiO_2 is that the valence band (VB) is predominantly composed of O - 2p orbitals and conduction band

(CB) primarily has Ti - 3d character as shown in the density of states (DOS) plot (see **Figure 1d**). So, when charge carriers are generated through photoexcitation or defect formation, they localize as hole polarons in the valence band, occupying O 2p states, and as electron polarons in the conduction band by filling up the empty Ti 3d states. **Figure 1(b)** shows the iso-surface charge density of a hole polaron in TiO_2 bulk. It is obvious from the shape of the orbital shown in **Figure 1b** that the hole polaron occupies O $2p_z$ orbitals. It is also evident from local lattice distortion around the polaronic site (**Figure 1c**) and magnetic moment of that specific site (**Figure S5**) that hole polaron forms at O-site. Due to hole localization as polaron, Ti – O^- bonds around the polaronic site become elongated by (0.10 – 0.13)Å compared to equilibrium Ti – O^{2-} bond length of undistorted geometry. The other Ti – O^{2-} bonds near the polaronic site elongated/shortened by only (0.02 – 0.09)Å compared to equilibrium Ti – O^{2-} bond length (see **Figure 1c**). The local distortion around the polaronic site happened due to the change of electrostatic interaction and modification of Ti (3d) – O (2p) orbital hybridization. The local distortion around the polaronic site along with hole trapping generates a local magnetic moment of approximately 0.68 μ_B at that specific O - atom (see **Figure S5**), within TiO_2 bulk. As a consequence of polaron formation, that particular O - atom changed its oxidation state from $O^{2-} \rightarrow O^{-}$ for hole polaron. This generates an extra electronic state within the band gap which is shown in **Figure 1e.**

Surface hole polaron geometry, stability, and energy levels

We now turn our discussion to surface hole polarons on rutile TiO_2 (110) clean surface. In this study, we stabilized hole polarons in five different O – sites separately; categorized as bulk, subsurface, axial, equatorial, and bridge hole polaron (see **Figure 2a**).

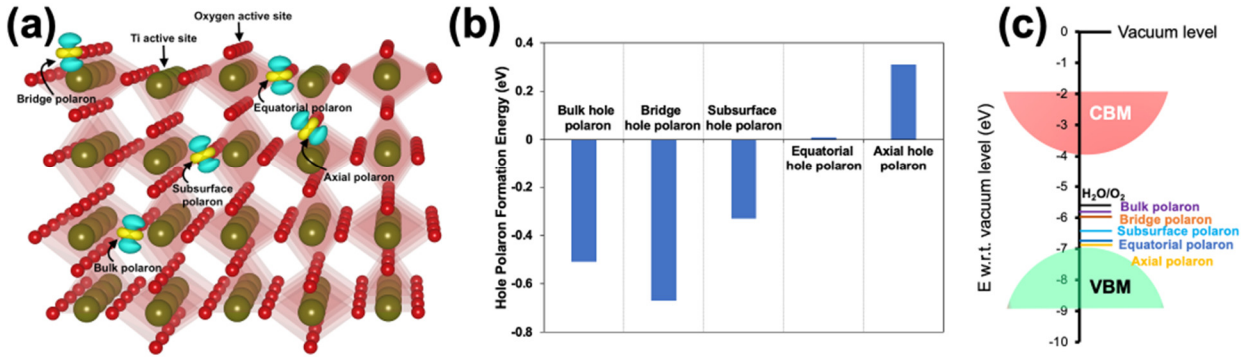

***Figure 2**. (a) Schematic diagram of different hole polaron configurations on (110) surface similar to Figure 1. (b) Thermodynamics of hole polaron formation energies at different configurations as shown in (a).(c) Schematic diagram of polaronic energy level for different hole polaron configurations with respect to band edges of TiO_2. The water redox potential (H_2O/O_2) is indicated as black solid line relative to vacuum at -5.67 eV.*

It is well known that the catalytic activity gets influenced by changes in the local environment, including oxidation state and bond length[33]. So, the simultaneous variation in oxidation state as well as Ti– O bond length in the vicinity of active site will significantly impact the OER reaction, a topic that will be discussed in a later section. **Figure 2(b)** shows the thermodynamic stability of a hole polaron at different configurations of TiO_2 (110) surface, where we used equation (1) to estimate the thermodynamic stability of the polaron. As described in the Computational Methods section, a negative polaron formation energy represents a stable (exothermic process) polaron and vice-versa. We have referenced the bulk hole polaron formation energy to a configuration where hole polaron is deep inside the surface. The estimated hole polaron formation energy in TiO_2 bulk is $-0.56\,eV$. On the other hand, the calculated hole polaron formation energy (from total DFT energies) for subsurface, axial, equatorial, and bridge O site hole polarons are $-0.33\,eV$, $0.31\,eV$, $0.01\,eV$, and $-0.67\,eV$, respectively. Clearly, bulk and bridge site hole polarons are thermodynamically the most stable. The subsurface (2nd layer) position is also the 2nd most stable polaron configuration followed by equatorial positions and then by the axial position as the least stable one among the configurations considered.

So far, we have discussed hole polaronic geometries and their thermodynamic stability. Now, we will discuss the relative position of hole polaronic states within the bandgap, as they play a crucial role in photocatalysis, optoelectronics, and other photo-driven applications. In general, the electronic structure of metal oxides relies on crystal symmetry, metal – oxygen bonding, and atomic orbital hybridization. An ideal crystal consists of filled valence band and unoccupied conduction band separated by a bandgap specific to the metal oxides. However, the presence of defects, like charge or point defects alters crystal symmetry, metal-oxygen bonding, and orbital hybridization. As a consequence, these defects in metal oxides create new electronic states within the bandgap. Like point defects, polarons also generate energy level within the bandgap. The relative position of polaronic energy level with respect to the band-edges depends on the degree

of charge localization and local lattice distortion. In this work, we estimated the relative position of hole polaronic energy levels of bulk as well as surface hole polarons in rutile TiO_2 **(Figure 2c)**. We first estimated the positions of hole polaronic energy levels with respect to the valence band edge from the respective density of states plots and then aligned them with respect to the common vacuum energy level. The details of the alignment with respect to common vacuum energy level was discussed in the supplementary information (see **SI Figure S8**). The estimated position of the bulk hole polaronic energy level is approximately 1.1 eV above the valence band maxima (VBM) (see the density of states plot in **SI Figure S9**). Through a nonempirical and self-consistent optimization of Hartree-Fock exchange, Elmaslmane et al.[57] also estimated the charge transition level (CTL) of bulk hole polaron at (1.18-1.23) eV above VBM in anatase TiO_2. In a similar fashion discussed above, we also estimated surface polaronic energy level of different hole polarons in rutile TiO_2 (110) surface. **Figure-2c** shows the relative position of hole polaronic states calculated with respect to the common vacuum energy level[58] (For detail, see **SI Figure S8**). Among all the hole polaron configurations considered for rutile TiO_2 (110) surface, the axial hole polaron generated a shallow polaronic level ($\Delta E \approx 0$) relative to valence band edge. Here, ΔE is the energy difference between polaronic state and valence band edge and determine the depth (shallow or deep) of the polaronic levels with respect to valence band edge. Equatorial hole polaronic level is located near to VBM ($\Delta E \approx 0.2$ eV). Unlike axial and equatorial hole polaron, subsurface and bridge hole polaron generate deep polaronic levels within the band gap. For subsurface and bridge hole polaron, ΔE is approximately 0.5 eV and 0.95 eV, respectively. The variation in the relative position of these polaronic levels originates from the fact that different polarons exhibit varying degrees of charge localization and local lattice distortion around the polaronic site.

Now, let's discuss the relative position of hole polaronic states with respect to H_2O/O_2 potential level, another key aspect of polaronic OER. The energy difference between hole polaronic state and H_2O/O_2 potential level determines the hole polaron transfer kinetics or the driving force for the transport of hole polarons to the OER active sites. The higher the energy difference, the higher the driving force. **Figure 2(c)** and SI **Figure S10(b)** show the schematic diagram of different hole polaronic states with respect to H_2O/O_2 potential. The axial, equatorial, subsurface, bridge, and bulk hole polarons are 1.29eV, 1.10 eV, 0.8eV, 0.35eV, and 0.2eV below H_2O/O_2 potential level, respectively. So, the axial and equatorial hole polarons will get sufficient energy to drive

themselves to the OER active sites. The subsurface hole polarons will have a moderate driving force. On the other hand, bridge, and bulk hole polarons will have insufficient energy to drive themselves to the OER reaction sites. Due to the relatively small energy difference between bridge and bulk polaronic state and H_2O/O_2 potential level, the transport of bridge and bulk hole polarons will be kinetically hindered during OER. The hinderance arises because they require at least ~(0.5-0.62) eV energy to overcome the site-to-site hoping barrier, as demonstrated by Deskins et al[30].

Therefore, the axial and equatorial hole polarons will be transported via polaron hopping by thermal fluctuations at room temperature, whereas the transport of bulk, subsurface, and bridge hole polarons to the reaction sites will be more challenging . However, surface, solvent, and thermal effects may modify the utility of such deep lying polarons which is not within the scope of this study and need further study.

OER mechanism with polaron on rutile TiO_2 (110) surface

The overall PEC water splitting reaction can be written as follows:

$$2H_2O(l) \rightarrow 2H_2(g) + O_2(g). \qquad (3)$$

The two half-reactions, water oxidation (oxygen evolution reaction, OER) occurring at the anode and water reduction (hydrogen evolution reaction, HER) taking place at the cathode, can be expressed as follows:

$$\textbf{Acidic OER:}\ 2H_2O \rightarrow O_2 + 4(H^+ + e^-) \qquad (4)$$

$$\textbf{Acidic HER:}\ 4H^+ + 4e^- \rightarrow 2H_2 \qquad (5)$$

As shown in equation (4), OER is protons coupled four electrons transfer (PCET) process, and each PCET requires at least 1.23 eV energy under standard equilibrium conditions. Therefore, the complete OER requires at least 4.92 eV minimum energy to split two H_2O molecules into one O_2 molecule. The overall acidic OER single site mechanism can be divided into four separate steps and can be written as follows:[14],[35]

$$\textbf{R1:}\ H_2O + * \rightarrow OH^* + (H^+ + e^-) \qquad (6)$$

$$\textbf{R2:}\ OH^* \rightarrow O^* + (H^+ + e^-) \qquad (7)$$

$$\textbf{R3:}\ O^* + H_2O \rightarrow OOH^* + (H^+ + e^-) \qquad (8)$$

$$\textbf{R4: } OOH^* \rightarrow * + O_2 + (H^+ + e^-), \qquad (9)$$

where the star symbol (*) represents an empty active site, and X* represents adsorbate X bonded with the empty active site. In order to determine OER free energy landscape, we calculated the Gibbs free energy change associated with each reaction involving intermediate adsorbates (OH*, O*, and OOH*) using previously developed method[14,59](See **SI Table-S4** for detail). The Gibbs free energy change for each reaction as shown in equation (6-9) can be written as follows:

$$\Delta G_{R1} = \Delta G_{HO*} - \Delta G_{H_2O(l)} - eU + k_B T\, ln(10)\text{pH} \qquad (10)$$

$$\Delta G_{R2} = \Delta G_{O*} - \Delta G_{HO*} - eU + k_B T\, ln(10)\ \text{pH} \qquad (11)$$

$$\Delta G_{R3} = \Delta G_{HOO*} - \Delta G_{O*} - eU + k_B T\, ln(10)\ \text{pH} \qquad (12)$$

$$\Delta G_{R4} = \Delta G_{O_2} - \Delta G_{HOO*} - eU + k_B T\, ln(10)\ \text{pH} \qquad (13)$$

Here, U represents the applied potential, and $k_B T\, ln(10)$ pH represents the pH correction term. It is important to mention that, in this work, we calculated Gibbs free energy change for reactions (6-9) at pH= 0, T = 298K, and under no applied potential i.e., $U = 0\,V$ vs. standard hydrogen electrode (SHE).

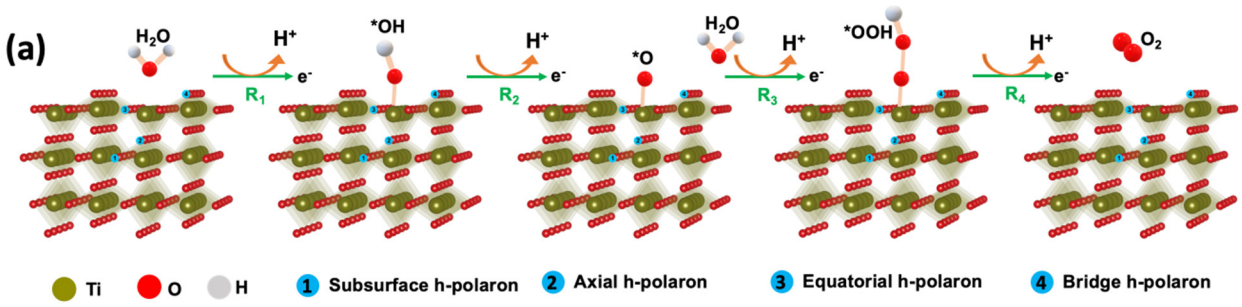

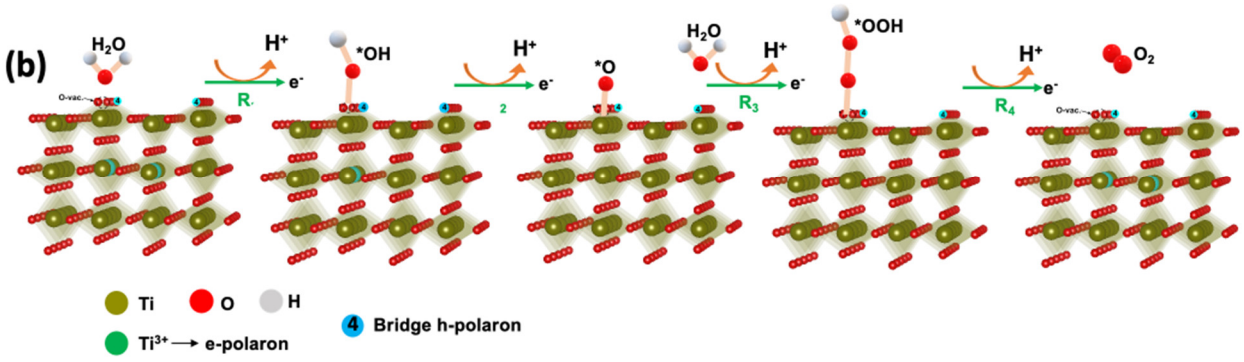

Figure 3*. Schematic diagram of OER pathway considered in this study. (a) OER at five coordinated Ti (Ti_{cus}) active site and (b) at two coordinated bridge oxygen (O_b) active site. OER at bridge oxygen site is associated with oxygen vacancy creation at bridge site which is shown by the black arrow. The creation of oxygen vacancy releases two extra electrons which eventually reduce two subsurface Ti – site (Ti^{3+}) and form electron polaron as indicated by the green-colored sphere. The oxygen sites which are indicated by 1-4 are the sites where hole polaron formation is considered in this study.*

Then the theoretical OER overpotential in Volts is then defined as:

$$\eta(V) = {Max(\Delta G_{R_i})}/{e} - 1.23\ V \qquad (14)$$

To understand hole polaronic OER, we studied OER on a clean TiO_2 (110) surface with and without a hole polaron. It is also important to note that the presence of a hole polaron represents OER under illuminated conditions, whereas its absence indicates OER under dark conditions. As mentioned above, the TiO_2 (110) surface consists of two OER active sites: the five coordinated Ti site (Ti_{cus}) and the two coordinated oxygen bridge-site (O_b) (see **Figure 2a**). In this study, we explored OER on both active sites separately. **Figure 3(a-b)** shows the OER mechanism involving the Ti_{cus} and the O_b active site, respectively. It is noteworthy to mention that we used a clean surface for the OER study because the surface Pourbaix diagram indicates that the clean surface is more stable than a *H and *OH covered surface (see **Figure S11**). However, hydroxylated surface, solvent or electrolyte can significantly impact the OER chemistry. This aspect falls outside the scope of the current investigation and requires further exploration.

For Ti_{cus} site OER, the Ti_{cus} site is involved in each step as shown in equation (6-9). However, OER at the O_b active site is initiated by a bridge site oxygen vacancy (shown in **Figure 3b** and **Figure 4**), which is subsequently occupied by OH from H_2O dissociation[34]. The subsequent OER steps closely resemble those observed at the Ti_{cus} site OER. It is important to note that the

bridge oxygen vacancy, created in the first step, releases two extra electrons. These electrons eventually form two electron-polarons located at two subsurface Ti atoms, reducing them from $Ti^{4+} \rightarrow Ti^{3+}$(see **Figure 4**). The electron-polaron formation at subsurface Ti sites in reduced TiO_2 (110) surface was previously confirmed experimentally[34] as well as theoretically[26,55].

Herein, we also benchmarked previously reported theoretical studies[26,55] of subsurface electron polaron formation at Ti sites in a reduced TiO_2 (110) surface (**Figure 4**). We explored different surface and subsurface Ti sites as the electron trapping center. Among all the configurations considered in this study, the lowest energy configuration agrees well with previously reported subsurface electron polaronic structure[26,55]. **Figure 4** shows the lowest energy subsurface electron polaronic structure with one oxygen (O_b) vacancy at bridge site. The details of subsurface electron polaron formation at different surface as well as subsurface Ti atoms are presented in the **Figure S12**. When an OH molecule attaches to the vacant site, it causes one of the subsurface Ti- polaronic sites with +3 oxidation state to oxidize into a Ti^{4+} state. Conversely, when an O binds to the vacant site, the remaining subsurface Ti^{3+} polaronic sites undergo oxidation to transition into Ti^{4+}. The original arrangement of the two subsurface Ti^{3+}polaronic sites is restored when an O_2 molecule leaves the surface in the final step of the OER reaction (see **Figure 3b**).

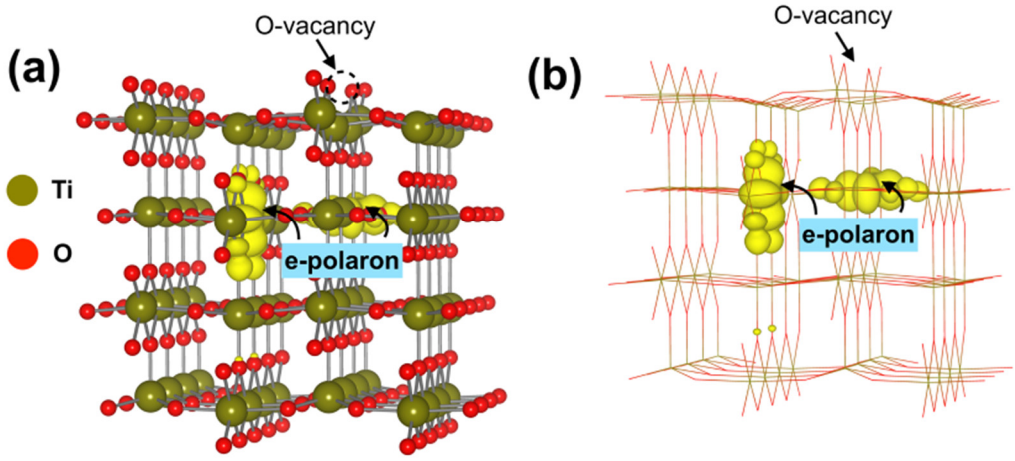

Figure 4*. Visualization of subsurface electron polaron at Ti-site. (a) Ball and stick model and (b) wire-frame model. The bridge oxygen vacancy on top of the surface is shown as black arrow and dotted circle. The yellow iso-surface represents electron polaron at Ti-site and the iso-surface is drawn with an iso-surface value of 0.005 eÅ^{-3}.*

For an ideal catalyst, the overpotential (η) is defined as zero, which means that $\Delta G_{R1} = \Delta G_{R2} = \Delta G_{R3} = \Delta G_{R4} = 1.23\, eV$. In the present study, we calculated the Gibbs free energy change and estimated the OER overpotential for scenarios both with and without hole polarons on the TiO_2 (110) surface. In **Figure-5(a-b),** we presented the computed OER free energy landscape for the Ti_{cus} and the O_b sites, respectively. In both scenarios, we established a baseline using a surface devoid of the hole polaron, representing what we term "dark conditions." From this baseline, we charted the free energy curves for the surfaces containing a hole polaron, representing illuminated conditions, at different O-sites (indicated by 1- 4) within the surface as shown in **Figure 3**. It is important to mention that during each of the polaronic OER steps as mentioned in equations (6-9), we performed a full relaxation of the system containing both hole polaron as well as adsorbate (e.g., HO*, O*, HOO*) on top of the surface. We allowed the adsorbates to relax in all directions as well as let the hole polarons to move within the surface during the geometry optimization. After full relaxation of the system, we confirmed the presence of hole polaron at desired configurations by analyzing the polaronic footprints mentioned above in the computational method section. Our results shows that hole polarons remains at the desired location during each of the polaronic OER steps.

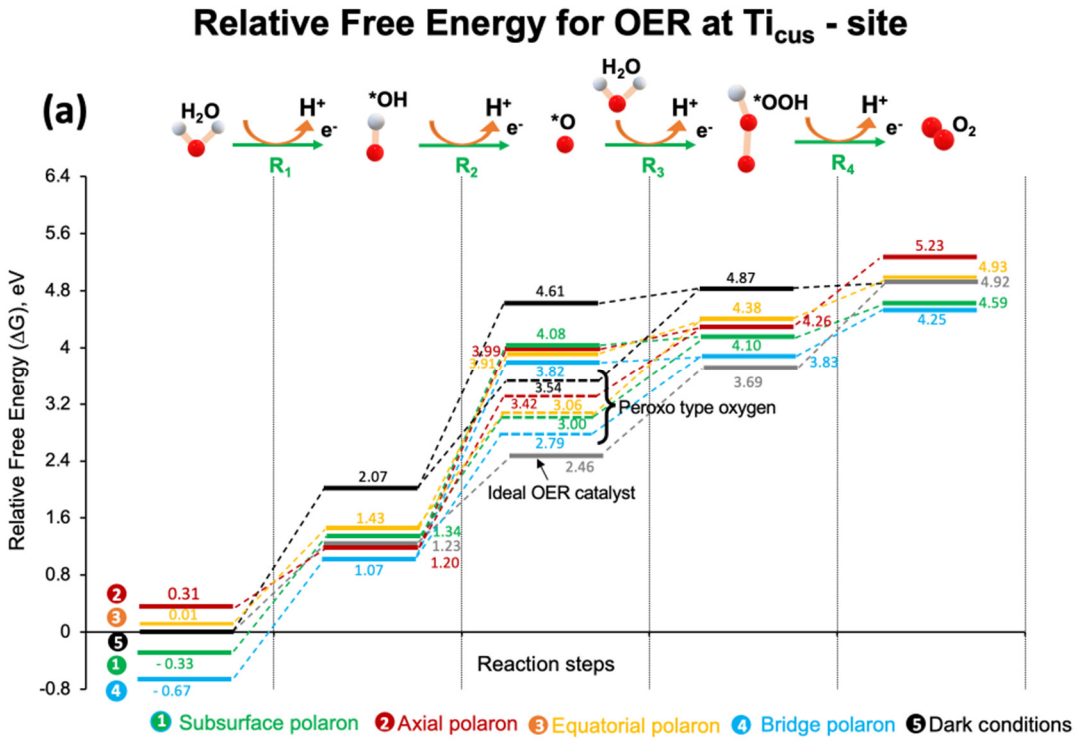

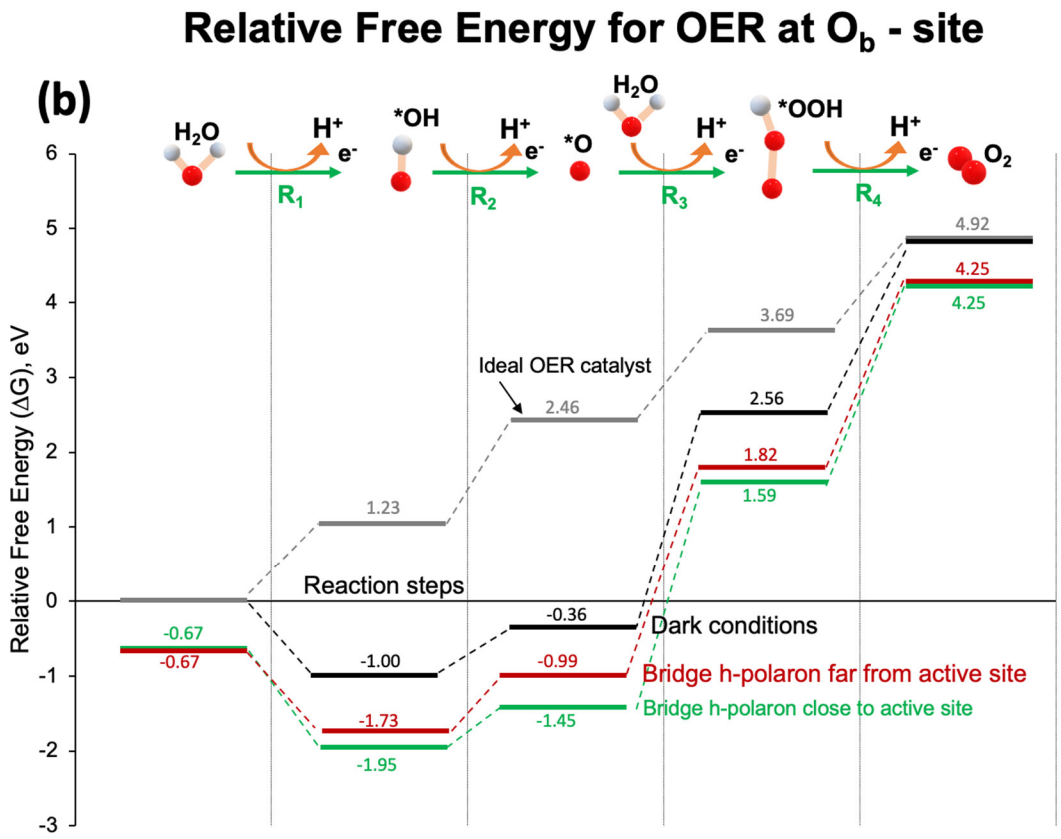

Figure 5*. Diagrams of relative free energy landscapes for OER pathways considered in this study. (a) OER at five coordinated Ti (Ti_{cus}) active site and (b) OER at two coordinated bridge oxygen (O_b) active site. The dashed lines serve as guide only. The calculated reaction energies for OER at both Ti_{cus} and O_b sites are presented in* ***Table S1****,* ***Table S2****, and* ***Table S3,*** *respectively.*

For Ti_{cus} site OER, we stabilized the hole polaron at four distinct positions (marked as 1- 4 in **Figure 3a and 5a**) separately and calculated the corresponding relative OER free energy. For the O_b site OER, we exclusively stabilized the hole polarons at the surface bridge site in two different locations – one positioned far from the active site and the other in the vicinity of the active site (see **Figures 3b and 5b**). As depicted in **Figure 5(a),** the presence of a hole polaron within the surface enhances the stability of *OH, regardless of its position for Ti-active site with *O on top. Conversely, *O becomes less stable with a surface hole polaron, except when the hole polaron is in an equatorial position. In equatorial polaron case, *O becomes slightly more stable compared to the scenario of without a hole polaron. Consequently, the difference in Gibbs free energy $\Delta G_{R2} (= \Delta G_{O*} - \Delta G_{OH*})$ is higher when a surface hole polaron is present, except in the case of

an equatorial position. As demonstrated in **Figure 5a,** step R2 emerges as the rate-determining step (RDS) for the Ti_{cus} site- OER. Therefore, all hole polaron configurations, excluding the equatorial one, increase the OER overpotential. Only the equatorial hole polaron reduces the OER overpotential by ~0.06eV compared to the absence of a hole polaron within the surface. Alongside the *O on top of Ti pathway, we also explored the surface peroxo oxygen pathway which was demonstrated as more stable configuration in rutile TiO_2 surface by Valdes et al.[35] We found that the OER overpotential for subsurface and bridge polaron configurations is significantly reduced by ~0.4eV through the surface peroxo oxygen pathway .

Analysis of the OER activity at the O_b site. Here, we exclusively focused on hole polarons at the surface bridge site, positioned in two ways – one farther from the active site and the other nearby. In **Figure 5b**, *OH exhibits greater stability regardless of the hole polaron's position. We find that O* becomes more stable when the hole polaron is near the active site but less stable when it is farther away. The situation is the opposite for *OOH, where a hole polaron far from the active site enhances stability compared to the scenario without a bridge hole polaron. As depicted in **Figure 5b**, step R3 serves as the rate-determining step (RDS), leading to a reduction in OER overpotential with a hole polaron positioned far from the active site, compared to the absence of a bridge hole polaron. This configuration lowers OER overpotential by ~0.12eV.

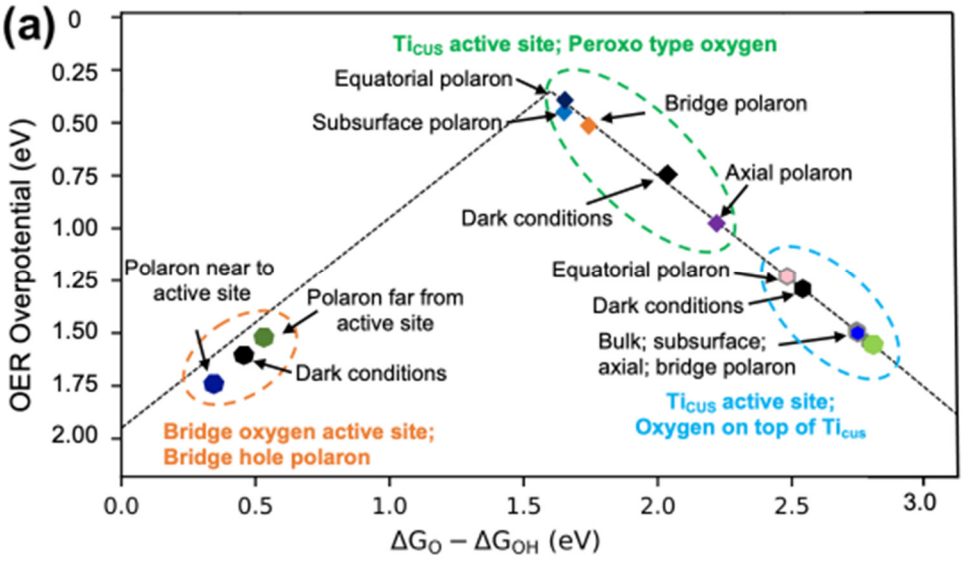

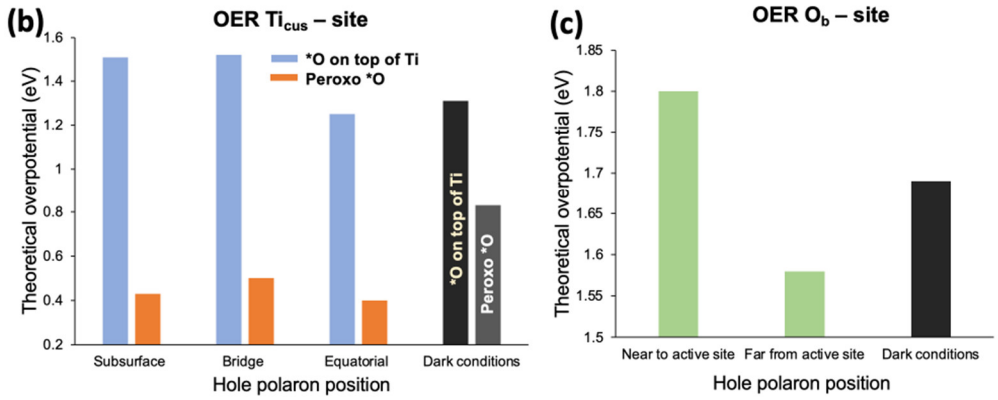

***Figure 6**. OER activity plots. (a) Volcano plot for OER onset potential. The left-hand side leg corresponds to O_b active site OER and right-hand side leg corresponds to Ti_{cus} active site OER. The volcano plot was plotted using the scaling relation presented in SI Figure 13, (b) OER overpotential for Ti_{cus} active site OER, and (c) OER overpotential for O_b active site OER. In all cases, dark conditions (without hole polaron) overpotential was considered as a reference.*

The impact of hole polarons on OER activity is further highlighted in the OER activity plot, shown in **Figure 6a**. This volcano type plot provides a visual representation of the changes in OER overpotential. The plot shows the surface associated with the equatorial hole polaron has a slight upward shift towards the top of the volcano (for oxygen on top of Ti_{cus} active site pathway). This slight upward shift signifies that hole polaron at this specific position decrease the OER overpotential. Indeed, this configuration reduced the OER overpotential by approximately 0.06eV compared to without the hole polaron scenario. On the other hand, for Ti_{cus} active site with peroxo type oxygen, the subsurface, bridge, and equatorial hole polarons reduced the OER overpotential significantly by approximately 0.4eV, which is shown by the upward shift of overpotential in the volcano plot. For O_b active site, hole polaron far away from active site, reduced the overpotential by ~0.12 eV compared to the dark conditions as illustrated in **Figures 6a,b,c**.

CONCLUSIONS

In this study, we applied DFT+U theory fitted to hybrid DFT to conduct a comprehensive simulations of surface polaron formation and describe the complex polaronic OER mechanism on a rutile TiO_2 (110) surface. We identify the thermodynamic stability of hole polarons at various oxygen sites, particularly emphasizing their propensity for bulk, bridge, and subsurface oxygen localization. The polaronic energy levels are deep within the bandgap for most of the hole polaron

configurations except the axial and equatorial hole polarons, which exhibited shallower behavior. These hole polarons were demonstrated to stabilize *OH and *O species on the surface, albeit with varied impacts on the OER overpotential. Notably, subsurface, bridge, and equatorial hole polarons reduced OER overpotential significantly by approximately 0.4eV for Ti_{cus} site OER via peroxo type oxygen pathway. Moreover, two other configurations showcased reduced overpotential in comparison to non-polaronic conditions. Hole polaron at equatorial (for Ti_{cus} site and oxygen on top OER) and far away bridge site (for O_b site OER) observes approximately 0.06eV and 0.12eV OER overpotential reduction, respectively. We have also shown that equatorial hole polaron has a shallow location near to the VBM which can be easily transported for use in OER. Surface bridge oxygen site in the OER mechanism involves subsurface electron polaron formation at Ti site during turnover. This study showed polaron induced significant OER enhancement, and it will offer important insights into polaronic OER within transition metal oxides and related metal chalcogenides. This work underscores the pivotal role of polarons in carrier separation and catalytic activity, holding promise for advancing PEC H_2O splitting technology and contributing to a carbon-free, green energy economy in the 21st century.

ACKNOWLEDGEMENT

This material is based on work performed by the Liquid Sunlight Alliance (LiSA), which is supported by the U.S. Department of Energy, Office of Science, Office of Basic Energy Sciences, Fuels from Sunlight Hub under Award DE-SC0021266. Computational resources were provided by the National Energy Research Scientific Computing Center (NERSC, account jcap), a DOE Office of Science User Facility supported by the Office of Science of the U.S. Department of Energy under contract No. DE-AC02-05CH11231.

DATA AVAILABILITY

All atomic configurations and DFT calculated energies are available in Catalysis Hub[60] under https://www.catalysis-hub.org/publications/Sarker Prediction2023.

REFERENCES

1. Grätzel, M. (2001) Photoelectrochemical cells. *Nature*, **414** (6861), 338–344.
2. Kunene, T., Xiong, L., and Rosenthal, J. (2019) Solar-powered synthesis of hydrocarbons from carbon dioxide and water. *Proc. Natl. Acad. Sci. U.S.A.*, **116** (20), 9693–9695.

3. Rahaman, M., Andrei, V., Wright, D., Lam, E., Pornrungroj, C., Bhattacharjee, S., Pichler, C.M., Greer, H.F., Baumberg, J.J., and Reisner, E. (2023) Solar-driven liquid multi-carbon fuel production using a standalone perovskite–BiVO4 artificial leaf. *Nat Energy*, **8** (6), 629–638.
4. Balzani, V., Pacchioni, G., Prato, M., and Zecchina, A. (2019) Solar-driven chemistry: towards new catalytic solutions for a sustainable world. *Rend. Fis. Acc. Lincei*, **30** (3), 443–452.
5. Lewis, N.S. (2016) Research opportunities to advance solar energy utilization. *Science*, **351** (6271), aad1920.
6. Peterson, A.A., Abild-Pedersen, F., Studt, F., Rossmeisl, J., and Nørskov, J.K. (2010) How copper catalyzes the electroreduction of carbon dioxide into hydrocarbon fuels. *Energy Environ. Sci.*, **3** (9), 1311.
7. Kuhl, K.P., Hatsukade, T., Cave, E.R., Abram, D.N., Kibsgaard, J., and Jaramillo, T.F. (2014) Electrocatalytic Conversion of Carbon Dioxide to Methane and Methanol on Transition Metal Surfaces. *J. Am. Chem. Soc.*, **136** (40), 14107–14113.
8. Li, C.W., Ciston, J., and Kanan, M.W. (2014) Electroreduction of carbon monoxide to liquid fuel on oxide-derived nanocrystalline copper. *Nature*, **508** (7497), 504–507.
9. Kudo, A., and Miseki, Y. (2009) Heterogeneous photocatalyst materials for water splitting. *Chem. Soc. Rev.*, **38** (1), 253–278.
10. Walsh, A., Ahn, K.-S., Shet, S., Huda, M.N., Deutsch, T.G., Wang, H., Turner, J.A., Wei, S.-H., Yan, Y., and Al-Jassim, M.M. (2009) Ternary cobalt spinel oxides for solar driven hydrogen production: Theory and experiment. *Energy Environ. Sci.*, **2** (7), 774.
11. Fujishima, A., and Honda, K. (1972) Electrochemical Photolysis of Water at a Semiconductor Electrode. *Nature*, **238** (5358), 37–38.
12. Thompson, T.L., and Yates, J.T. (2006) Surface Science Studies of the Photoactivation of TiO $_2$ New Photochemical Processes. *Chem. Rev.*, **106** (10), 4428–4453.
13. Nozik, A.J. (1975) Photoelectrolysis of water using semiconducting TiO2 crystals. *Nature*, **257** (5525), 383–386.
14. Man, I.C., Su, H., Calle-Vallejo, F., Hansen, H.A., Martínez, J.I., Inoglu, N.G., Kitchin, J., Jaramillo, T.F., Nørskov, J.K., and Rossmeisl, J. (2011) Universality in Oxygen Evolution Electrocatalysis on Oxide Surfaces. *ChemCatChem*, **3** (7), 1159–1165.
15. Lany, S. (2015) Semiconducting transition metal oxides. *J. Phys.: Condens. Matter*, **27** (28), 283203.
16. Yin, Z., Tordjman, M., Lee, Y., Vardi, A., Kalish, R., and Del Alamo, J.A. (2018) Enhanced transport in transistor by tuning transition-metal oxide electronic states interfaced with diamond. *Sci. Adv.*, **4** (9), eaau0480.
17. Setvin, M., Franchini, C., Hao, X., Schmid, M., Janotti, A., Kaltak, M., Van De Walle, C.G., Kresse, G., and Diebold, U. (2014) Direct View at Excess Electrons in TiO 2 Rutile and Anatase. *Phys. Rev. Lett.*, **113** (8), 086402.
18. Zhang, S.X., Kundaliya, D.C., Yu, W., Dhar, S., Young, S.Y., Salamanca-Riba, L.G., Ogale, S.B., Vispute, R.D., and Venkatesan, T. (2007) Niobium doped TiO2: Intrinsic transparent metallic anatase versus highly resistive rutile phase. *Journal of Applied Physics*, **102** (1), 013701.
19. Obara, Y., Ito, H., Ito, T., Kurahashi, N., Thürmer, S., Tanaka, H., Katayama, T., Togashi, T., Owada, S., Yamamoto, Y., Karashima, S., Nishitani, J., Yabashi, M., Suzuki, T., and

Misawa, K. (2017) Femtosecond time-resolved X-ray absorption spectroscopy of anatase TiO2 nanoparticles using XFEL. *Structural Dynamics*, **4** (4), 044033.
20. Yang, S., Brant, A.T., Giles, N.C., and Halliburton, L.E. (2013) Intrinsic small polarons in rutile TiO 2. *Phys. Rev. B*, **87** (12), 125201.
21. Krüger, P., Bourgeois, S., Domenichini, B., Magnan, H., Chandesris, D., Le Fèvre, P., Flank, A.M., Jupille, J., Floreano, L., Cossaro, A., Verdini, A., and Morgante, A. (2008) Defect States at the TiO 2 (110) Surface Probed by Resonant Photoelectron Diffraction. *Phys. Rev. Lett.*, **100** (5), 055501.
22. Moser, S., Moreschini, L., Jaćimović, J., Barišić, O.S., Berger, H., Magrez, A., Chang, Y.J., Kim, K.S., Bostwick, A., Rotenberg, E., Forró, L., and Grioni, M. (2013) Tunable Polaronic Conduction in Anatase TiO 2. *Phys. Rev. Lett.*, **110** (19), 196403.
23. Reticcioli, M., Setvin, M., Schmid, M., Diebold, U., and Franchini, C. (2018) Formation and dynamics of small polarons on the rutile TiO 2 (110) surface. *Phys. Rev. B*, **98** (4), 045306.
24. Selcuk, S., and Selloni, A. (2016) Facet-dependent trapping and dynamics of excess electrons at anatase TiO2 surfaces and aqueous interfaces. *Nature Mater*, **15** (10), 1107–1112.
25. Pastor, E., Sachs, M., Selim, S., Durrant, J.R., Bakulin, A.A., and Walsh, A. (2022) Electronic defects in metal oxide photocatalysts. *Nat Rev Mater*, **7** (7), 503–521.
26. Papageorgiou, A.C., Beglitis, N.S., Pang, C.L., Teobaldi, G., Cabailh, G., Chen, Q., Fisher, A.J., Hofer, W.A., and Thornton, G. (2010) Electron traps and their effect on the surface chemistry of TiO $_2$ (110). *Proc. Natl. Acad. Sci. U.S.A.*, **107** (6), 2391–2396.
27. Gono, P., Wiktor, J., Ambrosio, F., and Pasquarello, A. (2018) Surface Polarons Reducing Overpotentials in the Oxygen Evolution Reaction. *ACS Catal.*, **8** (7), 5847–5851.
28. Franchini, C., Reticcioli, M., Setvin, M., and Diebold, U. (2021) Polarons in materials. *Nat Rev Mater*, **6** (7), 560–586.
29. Deskins, N.A., Rousseau, R., and Dupuis, M. (2009) Localized Electronic States from Surface Hydroxyls and Polarons in TiO $_2$ (110). *J. Phys. Chem. C*, **113** (33), 14583–14586.
30. Deskins, N.A., and Dupuis, M. (2009) Intrinsic Hole Migration Rates in TiO $_2$ from Density Functional Theory. *J. Phys. Chem. C*, **113** (1), 346–358.
31. Deskins, N.A., and Dupuis, M. (2007) Electron transport via polaron hopping in bulk Ti O 2 : A density functional theory characterization. *Phys. Rev. B*, **75** (19), 195212.
32. De Lile, J.R., Bahadoran, A., Zhou, S., and Zhang, J. (2022) Polaron in TiO $_2$ from First Principles: A Review. *Advcd Theory and Sims*, **5** (2), 2100244.
33. Carneiro, L.M., Cushing, S.K., Liu, C., Su, Y., Yang, P., Alivisatos, A.P., and Leone, S.R. (2017) Excitation-wavelength-dependent small polaron trapping of photoexcited carriers in α-Fe2O3. *Nature Mater*, **16** (8), 819–825.
34. Zhang, Z., Bondarchuk, O., Kay, B.D., White, J.M., and Dohnálek, Z. (2006) Imaging Water Dissociation on TiO $_2$ (110): Evidence for Inequivalent Geminate OH Groups. *J. Phys. Chem. B*, **110** (43), 21840–21845.
35. Valdés, Á., Qu, Z.-W., Kroes, G.-J., Rossmeisl, J., and Nørskov, J.K. (2008) Oxidation and Photo-Oxidation of Water on TiO $_2$ Surface. *J. Phys. Chem. C*, **112** (26), 9872–9879.
36. Cheng, C., Zhu, Y., Fang, W.-H., Long, R., and Prezhdo, O.V. (2022) CO Adsorbate Promotes Polaron Photoactivity on the Reduced Rutile TiO $_2$ (110) Surface. *JACS Au*, **2** (1), 234–245.
37. Guzelturk, B., Winkler, T., Van De Goor, T.W.J., Smith, M.D., Bourelle, S.A., Feldmann, S., Trigo, M., Teitelbaum, S.W., Steinrück, H.-G., De La Pena, G.A., Alonso-Mori, R., Zhu, D.,

Sato, T., Karunadasa, H.I., Toney, M.F., Deschler, F., and Lindenberg, A.M. (2021) Visualization of dynamic polaronic strain fields in hybrid lead halide perovskites. *Nat. Mater.*, **20** (5), 618–623.
38. Lohaus, C., Klein, A., and Jaegermann, W. (2018) Limitation of Fermi level shifts by polaron defect states in hematite photoelectrodes. *Nat Commun*, **9** (1), 4309.
39. Wiktor, J., Ambrosio, F., and Pasquarello, A. (2018) Role of Polarons in Water Splitting: The Case of $BiVO_4$. *ACS Energy Lett.*, **3** (7), 1693–1697.
40. Rettie, A.J.E., Chemelewski, W.D., Lindemuth, J., McCloy, J.S., Marshall, L.G., Zhou, J., Emin, D., and Mullins, C.B. (2015) Anisotropic small-polaron hopping in W:BiVO4 single crystals. *Applied Physics Letters*, **106** (2), 022106.
41. Kresse, G., and Furthmüller, J. (1996) Efficiency of ab-initio total energy calculations for metals and semiconductors using a plane-wave basis set. *Computational Materials Science*, **6** (1), 15–50.
42. Hjorth Larsen, A., Jørgen Mortensen, J., Blomqvist, J., Castelli, I.E., Christensen, R., Dułak, M., Friis, J., Groves, M.N., Hammer, B., Hargus, C., Hermes, E.D., Jennings, P.C., Bjerre Jensen, P., Kermode, J., Kitchin, J.R., Leonhard Kolsbjerg, E., Kubal, J., Kaasbjerg, K., Lysgaard, S., Bergmann Maronsson, J., Maxson, T., Olsen, T., Pastewka, L., Peterson, A., Rostgaard, C., Schiøtz, J., Schütt, O., Strange, M., Thygesen, K.S., Vegge, T., Vilhelmsen, L., Walter, M., Zeng, Z., and Jacobsen, K.W. (2017) The atomic simulation environment—a Python library for working with atoms. *J. Phys.: Condens. Matter*, **29** (27), 273002.
43. Perdew, J.P., and Wang, Y. (1992) Accurate and simple analytic representation of the electron-gas correlation energy. *Phys. Rev. B*, **45** (23), 13244–13249.
44. Blöchl, P.E. (1994) Projector augmented-wave method. *Phys. Rev. B*, **50** (24), 17953–17979.
45. Anisimov, V.I., Zaanen, J., and Andersen, O.K. (1991) Band theory and Mott insulators: Hubbard *U* instead of Stoner *I*. *Phys. Rev. B*, **44** (3), 943–954.
46. Liechtenstein, A.I., Anisimov, V.I., and Zaanen, J. (1995) Density-functional theory and strong interactions: Orbital ordering in Mott-Hubbard insulators. *Phys. Rev. B*, **52** (8), R5467–R5470.
47. Dudarev, S.L., Botton, G.A., Savrasov, S.Y., Humphreys, C.J., and Sutton, A.P. (1998) Electron-energy-loss spectra and the structural stability of nickel oxide: An LSDA+U study. *Phys. Rev. B*, **57** (3), 1505–1509.
48. Heyd, J., Scuseria, G.E., and Ernzerhof, M. (2003) Hybrid functionals based on a screened Coulomb potential. *The Journal of Chemical Physics*, **118** (18), 8207–8215.
49. Fang, Y., Kong, X., Wang, D., Cui, S., and Liu, J. (2018) Role of dopant Ga in tuning the band gap of rutile TiO2 from first principles. *Chinese Journal of Physics*, **56** (4), 1370–1377.
50. Diebold, U. (2003) The surface science of titanium dioxide. *Surface Science Reports*, **48** (5–8), 53–229.
51. Morgan, B.J., and Watson, G.W. (2007) A DFT+U description of oxygen vacancies at the TiO2 rutile (110) surface. *Surface Science*, **601** (21), 5034–5041.
52. Pasumarthi, V., Liu, T., Dupuis, M., and Li, C. (2019) Charge carrier transport dynamics in W/Mo-doped $BiVO_4$: first principles-based mesoscale characterization. *J. Mater. Chem. A*, **7** (7), 3054–3065.
53. Liu, T., Zhou, X., Dupuis, M., and Li, C. (2015) The nature of photogenerated charge separation among different crystal facets of $BiVO_4$ studied by density functional theory. *Phys. Chem. Chem. Phys.*, **17** (36), 23503–23510.

54. Calzado, C.J., Hernández, N.C., and Sanz, J.Fdez. (2008) Effect of on-site Coulomb repulsion term U on the band-gap states of the reduced rutile (110) Ti O 2 surface. *Phys. Rev. B*, **77** (4), 045118.
55. Chrétien, S., and Metiu, H. (2011) Electronic Structure of Partially Reduced Rutile TiO_2 (110) Surface: Where Are the Unpaired Electrons Located? *J. Phys. Chem. C*, **115** (11), 4696–4705.
56. Sezen, H., Buchholz, M., Nefedov, A., Natzeck, C., Heissler, S., Di Valentin, C., and Wöll, C. (2014) Probing electrons in TiO2 polaronic trap states by IR-absorption: Evidence for the existence of hydrogenic states. *Sci Rep*, **4** (1), 3808.
57. Elmaslmane, A.R., Watkins, M.B., and McKenna, K.P. (2018) First-Principles Modeling of Polaron Formation in TiO_2 Polymorphs. *J. Chem. Theory Comput.*, **14** (7), 3740–3751.
58. Oba, F., and Kumagai, Y. (2018) Design and exploration of semiconductors from first principles: A review of recent advances. *Appl. Phys. Express*, **11** (6), 060101.
59. Rossmeisl, J., Qu, Z.-W., Zhu, H., Kroes, G.-J., and Nørskov, J.K. (2007) Electrolysis of water on oxide surfaces. *Journal of Electroanalytical Chemistry*, **607** (1–2), 83–89.
60. Winther, K.T., Hoffmann, M.J., Boes, J.R., Mamun, O., Bajdich, M., and Bligaard, T. (2019) Catalysis-Hub.org, an open electronic structure database for surface reactions. *Sci Data*, **6** (1), 75.